Chapter 5
Modeling of Transport Processes in Porous Materials

5.1 Introduction

As far as porous materials are characterized by high complexity in their *invisible internal structure*, modeling seems to be a grateful tool for understanding the transport processes that take place in porous media. Several modeling approaches, applicable in porous domain, have been introduced and used in a variety of scientific and industrial applications. Numerous industrial and technological applications involving fluid flow and mass transport processes within multi-particle assemblages have attracted scientific interest in recent decades. These focus mainly on industrial physicochemical processes (e.g. sedimentation, catalysis), alternative energy sources (e.g. fuel cells) and separation techniques (e.g. chromatography, filters). This chapter focuses on the modeling of mass transport in granular structures as well as on the estimation of macroscopic quantities (such as mass transport coefficient, adsorption efficiency, etc.).

5.2 Single Phase Transport in Unit Cells

Although arrays of regularly spatially distributed grains represent an idealization of real granular media, they have been widely studied from both the fluid dynamics and mass transport points of view. Due to their complex geometry, random particle distributions were the subject of few investigations until about twenty years ago. Since then, fast advances in computational capabilities have contributed to reviving research on this topic with emphasis on hydrodynamic aspects. Very often the particles are assumed to be sufficiently small and the physical properties of the fluid (i.e. viscosity and density) independent of the concentration of the transferred species, thus making it possible to uncouple the fluid problem from the mass-transport problem. Furthermore, the case of low Reynolds number flow is very important from an application point of view, where analytical solutions can be obtained for the flow field and the mass diffusion and/or adsorption process.

F. A. Coutelieris and J. M. P. Q. Delgado, *Transport Processes in Porous Media*, Advanced Structured Materials 20, DOI: 10.1007/978-3-642-27910-2_5,

5.2.1 Fundamental Quantities

Generally speaking, the transient mass transport of a passive solute in the void space of a porous medium is described by the convection–diffusion equation [4]:

$$\frac{\partial c_A}{\partial t} + \mathbf{v} \cdot \nabla c_A = D\nabla^2 c_A + R(c_A) \tag{5.1}$$

where c_A is the concentration of the passive solute, $\mathbf{v}$ is its velocity in the medium, D is its diffusivity in the intermediate occupying the medium's void space, and $R(c_A)$ describes the reactions taking place in the bulk phase.

For the sake of simplicity, the most common assumptions made in the relative literature and applied in the forthcoming analysis are:

- steady state condition (i.e. $\frac{\partial c_A}{\partial t} = 0$)
- inert bulk phase (i.e. $R(c_A) = 0$).

Consequently, the governing differential equation for mass transport in a porous material can often be written as:

$$\mathbf{v} \cdot \nabla c_A = D\nabla^2 c_A \tag{5.2}$$

The LHS of the above equation describes the mass transport *due to convection* while RHS stands for the mass transport *due to diffusion*. The relative dominance between these simultaneously occurring phenomena is expressed by the dimensionless *Peclet number*, defined as:

$$Pe = \frac{\text{characteristic velocity} \cdot \text{characteristic length}}{\text{diffusivity}} = \frac{U \cdot L}{D} \tag{5.3}$$

Obviously, the higher the Pe, the more convective the mass transport regime.

The microscopic quantity c_A is related to useful macroscopic quantities, such as the mass transport coefficient, the Sherwood (Nusselt) number, and the adsorption efficiency. A brief description of these quantities is given below.

The mass transport coefficient, k_0, describes the ability of the mass to be transferred from the bulk phase to solid absorbers. It is obviously dependant on the physical properties of the materials involved in the procedure, the porous structure, and some physical parameters such as pressure, temperature and volumetric flowrate, which could be considered critical for the process. Mathematically, the mass transport coefficient is defined by the expression:

$$k_0(\Delta c_A) S_{abs} = -\iint_{S_{abs}} [-N_A]_{surf} \, dS_{abs} \tag{5.4}$$

where Δc_A is the absolute difference of the concentration upon the absorbing surface S_{abs} from the incoming concentration, and $[-N_A]_{surf}$ is the component of molar flux which is normal on the collectors surface. The dimensionless overall

Sherwood number is a direct consequence of the mass transport coefficient and is defined as:

$$Sh_o = \frac{\text{mass transport coefficient} \cdot \text{characteristic length}}{\text{diffusivity}} = \frac{k_o \cdot L}{D} \tag{5.5}$$

For practical applications, the most useful macroscopic quantity is the adsorption efficiency, λ_0, defined by the ratio of the solute adsorption rate divided by the rate of the upstream influx:

$$\lambda_0 = 1 - \frac{\iint_{S_{outlet}} c_A \mathbf{v} \cdot \underline{n} dS}{\iint_{S_{inlet}} c_A \mathbf{v} \cdot \underline{n} dS} \tag{5.6}$$

where $\underline{\boldsymbol{n}}$ is the vector normal to the surface. For cases regarding the adsorption efficiency of a grain-in-cell, the above expression is modified to:

$$\lambda_0 = \frac{\iint_{S_{abs}} [-N_{A_r}]_{surf} dS_{abs}}{u_\infty c_{A,\infty} S_{inlet}} \tag{5.7}$$

where u_∞ is the approaching velocity, $c_{A,\infty}$ is the constant bulk concentration sufficiently far away from the collector surface, and S_{inlet} is the inlet surface that the solute faces to pass through the porous medium.

5.2.2 Adsorption Mechanisms

The majority of scientific and technological applications that deal with mass transport in porous materials, involve a *sorption mechanism*. Generally speaking, sorption includes adsorption and ion exchange, processes that involve the transfer and resulting equilibrium distribution of one or more solutes between a fluid phase and a solid surface. More precisely, adsorption generally involves the accumulation (or depletion) of solute molecules at an interface (gas–solid and liquid–solid interfaces), with solute distributed selectively between the fluid and solid phases. On the other hand, ion exchange occurs when positively (cations) or negatively (anions) charged ions from the fluid replace dissimilar ions of the same charge, being initially in the solid surface. Furthermore, the partitioning of a single solute between fluid and sorbed phases can be also included in the sorption mechanism.

Phase equilibrium between liquid and sorbed phases for one or many components in adsorption, or two or more species in ion exchange, is considered the single most important factor affecting process performance. This equilibrium is usually expressed by a boundary condition upon the liquid–solid interface, while it is of great importance to obtain a simple expression for the detailed description of the sorption mechanism. In relevant literature, several different cases for the adsorption of the solute upon the solid surface have been considered and used.

The first and simplest case corresponds to instantaneous adsorption upon the solid surface [17] and can be expressed as:

$$c_A = 0, \text{ on the solid}-\text{liquid interface} \tag{5.8}$$

Despite its mathematical simplicity, it is clear that the instantaneous adsorption approach pertains to a very limited range of applications, being a fairly rare physicochemical phenomenon. Thus, detailed models referring to adsorption following isotherms have also been adopted. The most common is that of Langmuir's isotherm, which can be formulated as [12]:

$$D\underline{\boldsymbol{n}} \cdot \nabla c_A = \frac{k}{K} c_s, \text{ on the solid}-\text{liquid interface} \tag{5.9}$$

where c_s is the concentration of the sorpted material, K is a constant defined by the Langmuir isotherm:

$$\Theta_{eq} = \frac{Kc_b}{1 + Kc_b} \tag{5.10}$$

and k is a reaction rate defined from the relation

$$R(c_s) = kc_b(c_{mx} - c_s) \tag{5.11}$$

where $R(c_s)$ is the overall adsorption rate given as a function of the surface concentration c_s, c_b is the concentration of the diluted mass in the neighborhood of the solid surface, c_{mx} is the maximum concentration attained when the surface is completely covered by substance A, and Θ_{eq} is the ratio of the covered to the total surface, defined as:

$$\Theta_{eq} = \frac{c_s}{c_{mx}} \tag{5.12}$$

Another more detailed approach is the more complicated but realistic sorption mechanism, which involves adsorption-reaction-desorption [13]. More specifically, it can be considered that the solute diluted in the bulk phase is initially adsorbed by the solid surface where a heterogeneous reaction takes place, and its products, assumed to be inactive and of very low concentrations, are again desorbed in the bulk phase. The adsorption is assumed to occur due to vacant sites [2] that are normally distributed over the surface area while the whole process is determined by an overall rate according to thermodynamics. The above mechanism is often described by an expression of the form:

$$D\underline{\boldsymbol{n}} \cdot \nabla c_A = R_n, \text{on the solid}-\text{liquid interface} \tag{5.13}$$

With R_n denoting the overall adsorption rate, given as:

$$R_n = k_s c_{AS}^n \tag{5.14}$$

where k_s is the rate constant of the heterogeneous reaction upon the surface, and the concentration of solute on the solid surface, c_{AS}, is calculated by solving the non linear equation:

$$k_s c_{AS}^n + \left[k_A^d + k_A^a c_A)_{surf} N\right] c_{AS} - k_A^a c_A)_{surf} \xi_m = 0 \tag{5.15}$$

Equation 5.15 correlates the hard-to-measure surface concentration of A, c_{AS}, with its concentration in the bulk phase very close to the solid surface $c_A)_{surf}$ by considering the balance for the active sites on the adsorbing surface. In the above equation, the terms $k_A^a$and k_A^ddenote the adsorption and desorption rate constants of solute, respectively, ξ_m is the concentration of the vacant sites of the solid surface, and N is Avogadro's number, while n denotes the order of the heterogeneous reaction upon the surface. In general, only the cases of $n = 0$, $n = 1$ and $n = 2$ are of practical importance, but zero order reactions are also used in limited applications [2].

Finally, it should be noted that some models consider neutral solid surface i.e. absolute absence of adsorption [11]. This case can be described by the following boundary condition upon the solid surface:

$$\underline{\boldsymbol{n}} \cdot \nabla c_A = 0, \text{ on the solid}-\text{liquid interface} \tag{5.16}$$

5.2.3 Mass Transport Through Spheres

As discussed in Sect. 2.2, sphere-in-cell geometry is a simple model that represents the actual complex geometry of the pore space in spherical particle assemblages and the approximation of the flow-field therein. Consider a typical sphere-in-cell model where the approaching fluid is a dilute solution of a substance A, which is moving towards the solid adsorbing surface. After taking into account the plane symmetry of the problem, the governing equation for the steady state mass transport in the fluid phase within the model can be written in spherical coordinates (r, θ) as:

$$u_r \frac{\partial c_A}{\partial r} + \frac{u_\theta}{r} \frac{\partial c_A}{\partial \theta} = D\left(\frac{\partial^2 c_A}{\partial r^2} + \frac{2}{r}\frac{\partial c_A}{\partial r} + \frac{1}{r^2}\frac{\partial^2 c_A}{\partial \theta^2} + \frac{\cot\theta}{r^2}\frac{\partial c_A}{\partial \theta}\right) \tag{5.17}$$

where u_r and u_θ are the $r-$ and $\theta-$velocity components, given either by Eqs. 3.12 and 3.13 or by Eqs. 3.19 and 3.20, where the set chosen depends on the model considered.

The axial symmetry of the mass transfer problem is expressed by the following boundary conditions:

$$\left.\frac{\partial c_A}{\partial \theta}\right]_{\theta=\pi} = 0, \quad a < r \leq \beta \tag{5.18}$$

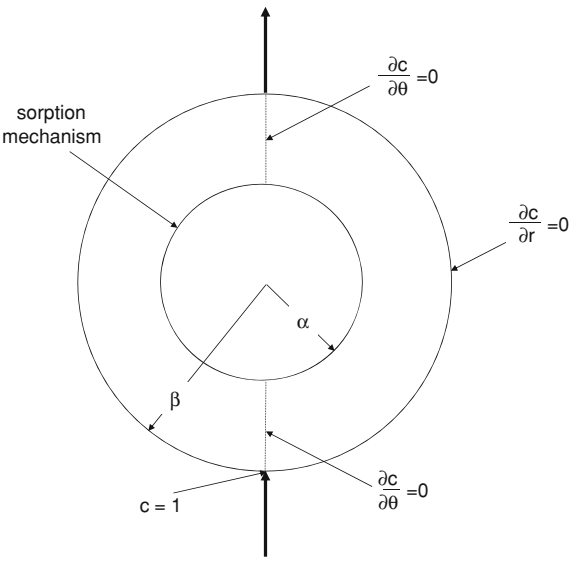

Fig. 5.1 Mass transport taking place in a sphere-in-cell. *Bold arrows* indicate flow direction

$$\left.\frac{\partial c_A}{\partial \theta}\right]_{\theta=0} = 0, \quad a < r \leq \beta \tag{5.19}$$

To ensure the continuity of concentration for any Peclet number, Coutelieris et al. [9] proposed the following boundary condition at the outer boundary of the cell:

$$c_A(r = \beta, \theta = \pi) = 1 \tag{5.20}$$

$$\left.\frac{\partial c_A}{\partial r}\right]_{r=\beta} = 0, \quad 0 \leq \theta < \pi \tag{5.21}$$

For high Peclet values, the boundary condition (5.20) and (5.21) is completely equivalent to the well-known Levich approach for unbounded fluids, given elsewhere as [8, 17]:

$$c_A = 1, \quad \text{for } r \to \infty \quad \text{or} \quad r = \beta \tag{5.22}$$

Figure 5.1 shows the extent of the concentration boundary layer surrounding the solid surface.

There are several approaches for describing the sorption mechanism (see Sect. 5.2.2). By using the geometrical specification of the sphere-in-cell model, sorption in specific spherical geometries can be written as follows:

$$[(5.16)\ \text{neutral surface}] \Rightarrow \left.\frac{\partial c_A}{\partial r}\right]_{r=\alpha} = 0, \quad 0 \leq \theta < \pi \tag{5.23}$$

$$[(5.8)\ \text{instantaneous adsorption}] \Rightarrow c_A(r = a, \theta) = 0,\ 0 \leq \theta \leq \pi \tag{5.24}$$

$$[(5.9)\ \text{Langmuir isotherm}] \Rightarrow D\frac{\partial c_A}{\partial r}\Bigg]_{r=\alpha} = \frac{k}{K}c_s, \quad 0 \le \theta \le \pi \tag{5.25}$$

$$[(5.13)\ \text{adsorpionndash;reactionndash;desorption}] \Rightarrow D\frac{\partial c_A}{\partial r}\Bigg]_{r=\alpha} = R_n,\ 0 \le \theta \le \pi \tag{5.26}$$

At high *Pe* numbers, the above described mass transport problem (considering each possible adsorption case) is amenable to analytical treatment with sufficient accuracy, as shown by various research groups [8, 17]. Mathematically, it is notable here that the RHS of Eq. 5.2 is simplified enough to accept a variables' separated function as an analytical solution. This is because the concentration boundary layer is very thin compared to the local radius of curvature of the particle, therefore the curvature term and the tangential diffusion terms can be neglected. In particular, Eq. 5.2 becomes:

$$u_r\frac{\partial c_A}{\partial r} + \frac{u_\theta}{r}\frac{\partial c_A}{\partial \theta} = D\frac{\partial^2 c_A}{\partial r^2} \tag{5.27}$$

which is parabolic on θ and can be solved analytically in a manner quite similar to that of Levich [17]. By using dimesionless quantities, the concentration profile in the fluid phase is of the form:

$$c_A(z) = c_2\int_0^z e^{-\frac{4}{9}t^3}dt + c_3 \tag{5.28}$$

where:

$$z = \sqrt[3]{\frac{3\,Pe}{4\alpha^3}}\,r\,\frac{\sin\theta}{\theta - 0.5\sin 2\theta} \tag{5.29}$$

and c_2 and c_3 are coefficients that can impose the appropriate boundary conditions for mass transport.

For the case of low and moderate Peclet numbers, all the terms of the transport equation (5.17) survive, therefore it is necessary to apply numerical approaches to obtain the solution. What is important for cases of low Peclet number is the boundary condition on the outer boundary, as described by Eqs. 5.20 and 5.21, is equivalent to that of Levich for high Peclet numbers, while it allows the boundary layer to violate the concept of a very thin boundary layer imposed by the Levich approach [17]. The difference between high and low Peclet mass transport in sphere-in-cell geometry, is graphically summarized in Fig. 5.2.

Obviously, mass transport problems assuming neutral solid grains (no adsorption) result in a uniform concentration profile without scientific or industrial interest. For instantaneous adsorption and using Kuwabara's approach for the velocity field, the concentration profiles for a moderate Peclet value (Pe = 70) are presented in Fig. 5.3.

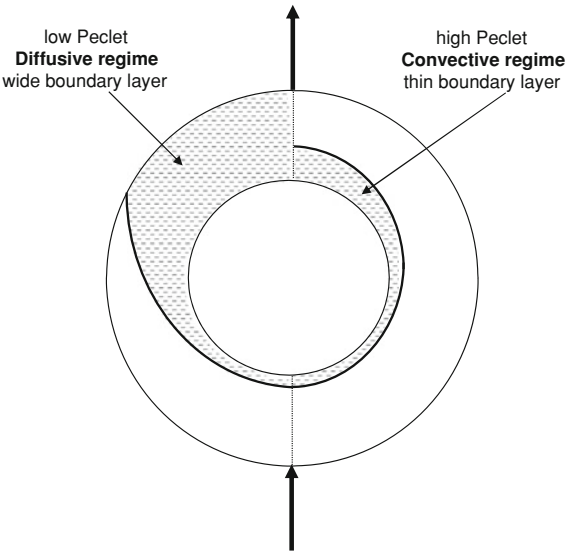

Fig. 5.2 Schematic visualization of boundary layers for low and high Peclet numbers

For Langmuir-type adsorption with the same geometry and flow conditions, the concentration profiles are shown in Fig. 5.4.

It should be stressed however, that the boundary condition (5.26) in combination with (5.14)–(5.15), imply non-linearity in the whole approach and, therefore, an iterative numerical technique is necessary to obtain the solution. Thus, the integration of the transport equation must be numerical, although the flow field can be obtained analytically through Happel or Kuwabara type boundary conditions. Figure 5.5 visualizes the concentration profiles for the realistic sorption mechanism with the same geometry and flow conditions as those for the other adsorption types, presented above.

The above Figs. 5.3, 5.4 and 5.5 show a gradual decrease of the concentration for constant r as the angular position approaches the outlet because of the shape and extent of the concentration boundary layer. Therefore, the possibility for the solute to be captured by the solid surface decreases with angular position because of the convective regime. In general, higher concentration gradients at any radial and angular positions are found in cases of instantaneous adsorption compared to those for other sorption mechanisms, as the surface concentration, $c_A(\alpha,\theta)$, is much higher in the cases of Langmuir type or realistic adsorption mechanisms, taking its highest value at the impact point and decreasing monotonically as θ tends to π.

For all sorption mechanisms considered, the overall Sherwood number, Sh_o, is calculated as follows [6]:

$$Sh_o = \frac{1}{4\pi a^2} \int_{\pi}^{0} \frac{\left(\frac{\partial c_A}{\partial r}\right)_{r=a}}{c_A(\beta,\theta) - c_A(\alpha,\theta)} d\theta \tag{5.30}$$

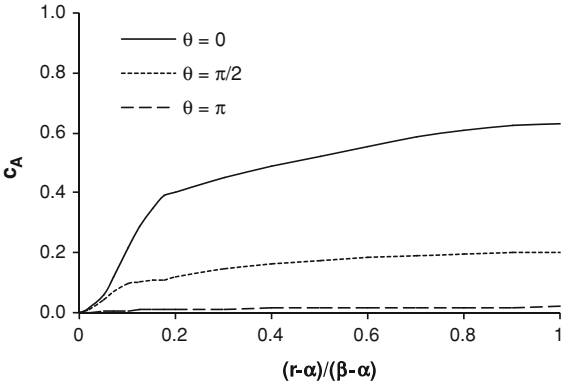

Fig. 5.3 Spatial concentration profiles for $\varepsilon = 0.9$ at three different angular positions of the sphere-in-cell for instantaneous adsorption

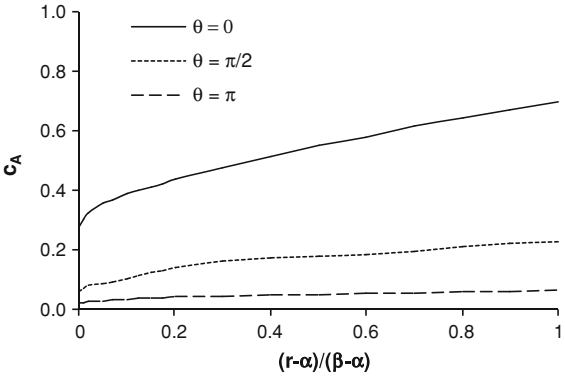

Fig. 5.4 Spatial concentration profiles for $\varepsilon = 0.9$ at three different angular positions of the sphere-in-cell for Langmuir type adsorption $\left(\frac{k}{K} = 1\right)$

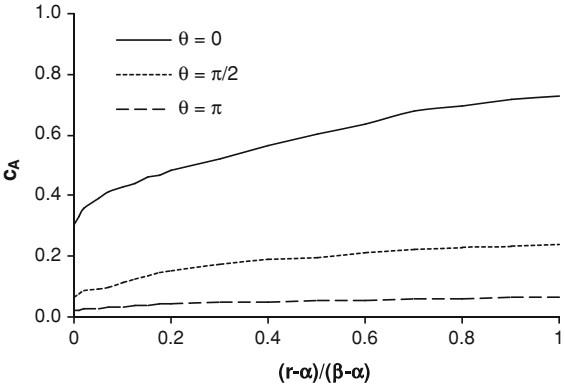

Fig. 5.5 Spatial concentration profiles for $\varepsilon = 0.9$ at three different angular positions of the sphere-in-cell for realistic sorption mechanism

Finally, the adsorption efficiency of a sphere-in-cell model can be written as:

$$\lambda_0 = \frac{\iint\limits_{S_{sphere}} [-N_{A_r}]_{r=a} dS_{sphere}}{u_\infty c_{A,\infty} 4\pi\beta^2} \tag{5.31}$$

where it can be easily shown for the specified spherical geometry that:

$$\lambda_o = \frac{a^2}{4\pi\beta^2} \int_0^\pi \sin\theta \left(\frac{\partial\left(\frac{c_A}{c_{A,\infty}}\right)}{\partial\left(\frac{r}{\alpha}\right)} \right)_{r=\alpha} d\theta \tag{5.32}$$

To initially investigate the macroscopic behavior of the sphere-in-cell model, Fig. 5.6 presents the overall Sherwood number as a function of the Peclet number for a relatively high porosity value ($\varepsilon = 0.9$) in the case of instantaneous adsorption. An almost monotonic increment of Sh_o is observed as the Peclet values increase. This is due to the higher concentration gradients close to the adsorbing surfaces in highly convective regimes. It has been also shown that such analytical results are in very good agreement with experimental measurements and numerical simulations [11]. This agreement can be attributed to the high porosity value used, taking into account that the analytical approach has been shown to be highly accurate in that range [5, 9, 26]. High porosity values favor the accuracy of transport results because mass transport under high Peclet values develops very thin boundary layers, a consideration which corresponds to an outer sphere of radius significantly higher than the inner one, i.e. porosity takes quite high values. To further clarify the situation, the dependence of the overall Sherwood number on porosity for the case of instantaneous adsorption is shown in Fig. 5.7. Evidently, increasing porosities do not favor mass exchange efficiency and the Sh_o drops. High porosity values correspond to low available surface for mass transfer leading to low adsorption rates for the porous material. Again experimental data and numerical predictions are generally in agreement with the analytical results [11] although an erratic behavior is observed. This behavior is due to the fact that high porosities, where analytical models are in principle applicable, correspond to a very low number of spheres for the numerical representation of the porous medium. It should be noted that at porosities lower than 0.8, the available analytical approaches become gradually less accurate and therefore less dependable.

To include the more detailed and realistic sorption mechanism of Eqs. 5.26, 5.14 and 5.15 into the whole approach, it is necessary to numerically solve the boundary value problem described above either using the Kuwabara or Happel expression for the velocity components. Frequently, a non-uniform finite-difference scheme is employed where the value of λ_0 can be calculated once the radial component of the concentration gradient upon the surface is known by using a numerical integration method (the most suitable choice could be the modified Newton–Cotes with an adjustable step). The effect of the sorption mechanism

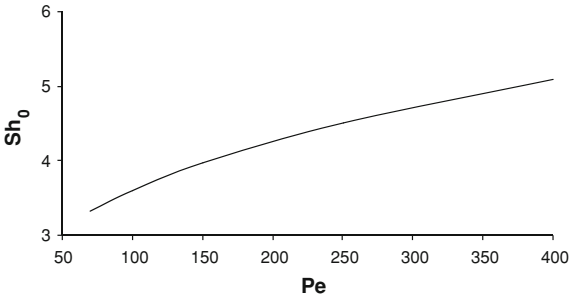

Fig. 5.6 Dependence of the overall Sherwood number on the Peclet for a high porosity value (instantaneous adsorption)

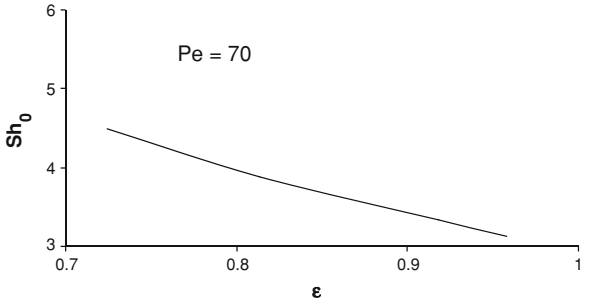

Fig. 5.7 Influence of the porosity on the overall Sherwood number (instantaneous adsorption)

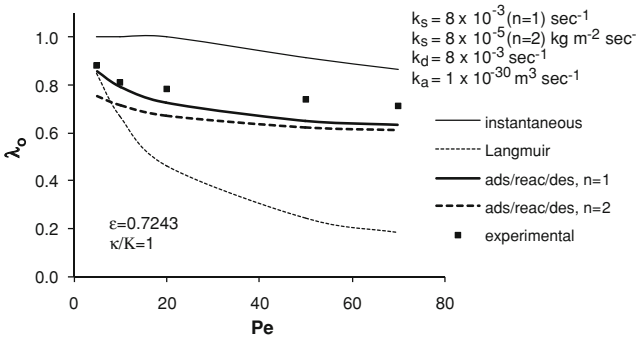

Fig. 5.8 Adsorption efficiency of the sphere-in-cell model as a function of Pe for several adsorption mechanisms, compared to experimental data presented by discrete points [29]

considered, is clearly depicted in Fig. 5.8, which presents the adsorption efficiency as a function of Pe for various adsorption mechanisms.

In general, higher efficiency is found for instantaneous adsorption than for the Langmuir type, as the concentration gradients are lower in the latter case. Indeed, in Langmuir adsorption concentration on the solid surface attains non zero values thus rendering the overall driving force $c_A(\beta,\theta) - c_A(a,\theta)$ smaller. A general decrement of the efficiency with Peclet is observed, a trend expected as the more convective flows (increasing Peclet) tend to prevent solute from being captured by the solid surface. The discrete points represent the experimental data of Wilson and Geankoplis [29] for the rather high porosity of 0.7 (the highest porosity used in

their experiments). As these authors measured the overall Sherwood number, it is necessary to transform it into adsorption efficiency to allow direct comparison with the predictions. Starting from the definition of adsorption efficiency in Eq. 5.31 the numerator (r-component of the molar flux on the adsorbing surface) can be expressed by the use of the mass transfer coefficient as $k_0 \cdot \Delta C \cdot S_{sphere}$. After some algebraic manipulations, this leads to the following linear relation between the overall Sherwood number and λ_0:

$$Sh = \lambda_0 \frac{Pe}{(1-\varepsilon)} \frac{a}{L} \frac{c_{A.\infty}}{\langle c_A \rangle} \tag{5.33}$$

where $\langle c_A \rangle$ is the spatially averaged concentration of solute, and L is the characteristic length, used when defining the Peclet number (see Eq. 5.3) As the experimental adsorption mechanism is not clearly known, the agreement between predictions and experimental data is considered sufficient.

5.2.4 Mass Transport Through Cylinders

The 2-D sphere-in-cell models are completely equivalent to 2-D cylinder-in-cell models. For this reason, the solutions of the previous Sect. 5.2.3 are valid for both cases.

5.2.5 Mass Transport Through Spheroids

Spheroidal geometry was more difficultly approached until the 1990s than spherical one because the flow field had to be estimated numerically, even for creeping flow conditions. This is because the governing Eq. 3.9 in terms of stream function is not separable in spheroidal coordinates whereas it is separable in Cartesian, cylindrical and spherical ones. In 1994, Dassios et al. [14] overcome this barrier by introducing the method of variable semi-separation, thus obtaining analytical expressions for the velocity components when either Happel or Kuwabara type boundary conditions were considered. (For a detailed description of the spheroid-in-cell model, see Sect. 3.2.4.)

By considering this cell approach, the governing equation for steady state mass transport in the fluid phase within the model can be written in prolate spheroidal coordinates (η, θ) as:

$$u_\eta \frac{\partial c_A}{\partial \eta} + u_\theta \frac{\partial c_A}{\partial \theta} = \frac{D}{\alpha \sqrt{\sinh^2 \eta + \sin^2 \theta}} \cdot \left(\frac{\partial^2 c_A}{\partial \eta^2} + \coth \eta \frac{\partial c_A}{\partial \eta} + \frac{\partial^2 c_A}{\partial \theta^2} + \cot \theta \frac{\partial c_A}{\partial \theta} \right) \tag{5.34}$$

where u_η and u_θ are the $\eta-$ and $\theta-$velocity components, depend on the model considered (Happel or Kuwabara type boundary conditions).

The axial symmetry of the mass transfer problem is assured by the boundary conditions (5.18) and (5.19), where the continuity of concentration for any Peclet number is described by the boundary condition at the outer boundary of the cell [10]:

$$c_A\left(\eta = \eta_\beta, \theta = \pi\right) = 1 \tag{5.35}$$

$$\left.\frac{\partial c_A}{\partial \eta}\right]_{\eta=\eta_\beta} = 0, \quad 0 \le \theta < \pi \tag{5.36}$$

Again several approaches for describing the sorption mechanism can be adopted (see Sect. 5.2.2), as follows:

$$[(5.16)\text{ neutral surface}] \Rightarrow \left.\frac{\partial c_A}{\partial \eta}\right]_{\eta=\eta_a} = 0, \quad 0 \le \theta < \pi \tag{5.37}$$

$$[(5.8)\text{ instantaneous adsorption}] \Rightarrow c_A(\eta = \eta_a, \theta) = 0, \quad 0 \le \theta \le \pi \tag{5.38}$$

$$[(5.9)\text{ Langmuir isotherm}] \Rightarrow \frac{D}{\alpha\sqrt{\sinh^2\eta_\alpha + \sin^2\theta}}\left.\frac{\partial c_A}{\partial \eta}\right]_{\eta=\eta_a} = \frac{k}{K}c_s, \quad 0 \le \theta \le \pi \tag{5.39}$$

$$[(5.13)\text{ adsorpionndash;reactionndash;desorption}] \Rightarrow \frac{D}{\alpha\sqrt{\sinh^2\eta_\alpha + \sin^2\theta}}\left.\frac{\partial c_A}{\partial r}\right]_{r=\alpha} = R_n, \quad 0 \le \theta \le \pi \tag{5.40}$$

As shown above, the consideration of high Pe numbers corresponds to the analytical solution to the mass transport problem [8, 10]. The assumption of a very thin boundary layer leads to a transformed formation of Eq. 5.34 as follows:

$$u_\eta \frac{\partial c_A}{\partial r} + u_\theta \frac{\partial c_A}{\partial \theta} = \frac{D}{\alpha\sqrt{\sinh^2\eta_\alpha + \sin^2\theta}}\frac{\partial^2 c_A}{\partial \eta^2} \tag{5.41}$$

which can be solved analytically in a manner similar to that of Levich [17], providing concentration profiles in the fluid phase of the form given by (5.28) while the transformed variable z is given as:

$$z = \left[\frac{\alpha \mathrm{K}\, Pe}{4\Lambda \sinh^2\eta_a}\right]^{\frac{1}{3}} \eta \frac{\sin\theta}{\left[\frac{\sin 2\theta}{4} - \frac{\theta}{2}\right]^{\frac{1}{3}}} \tag{5.42}$$

where K and Λ are given by Coutelieris et al. [8]. Whenever Peclet attains low or moderate values, a numerical approach must be involved, as discussed previously.

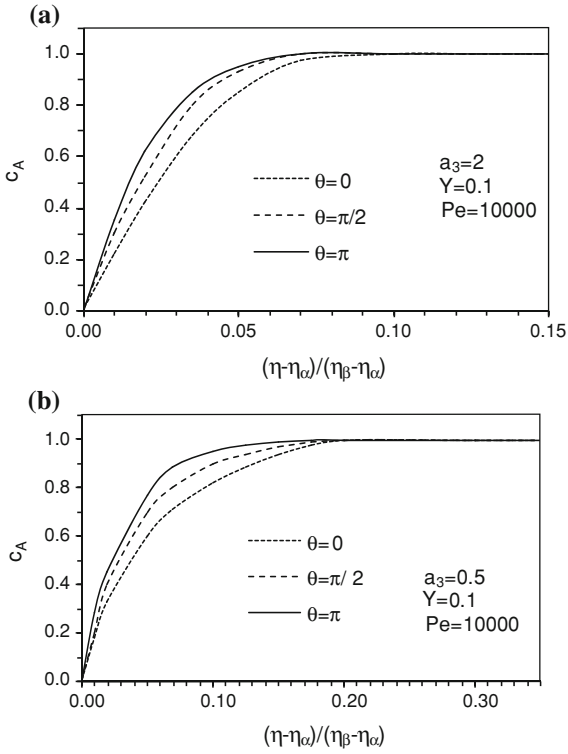

Fig. 5.9 Concentration profiles in the vicinity of adsorbing prolate (**a**) and oblate (**b**) spheroids-in-cell at three different angular positions for instantaneous adsorption and high Pe

By employing the transformation for the oblate spheroidal coordinates, given by (3.38) and (3.39), the concentration profile is again described by (5.28), where:

$$z = \left[\frac{\bar{\alpha}\,\bar{\mathrm{K}}\,Pe}{4\bar{\Lambda}\left(\sinh^2\bar{\eta}_a+1\right)}\right]^{\frac{1}{3}}\bar{\eta}\,\frac{\sin\theta}{\left[\dfrac{\sin 2\theta}{4}-\dfrac{\theta}{2}\right]^{\frac{1}{3}}} \tag{5.43}$$

and $\bar{\mathbf{K}}$, $\bar{\mathbf{\Lambda}}$ are given by Coutelieris et al. [8].

Again the assumption of neutral solid grains clearly results in a uniform concentration profile that lacks scientific interest. For instantaneous adsorption and using Kuwabara's approach for the velocity field, the concentration profiles for a high Peclet value (Pe = 10,000) are presented in Fig. 5.9.

The assumption of instantaneous adsorption for *low* Peclet values corresponds to the concentration profiles in Fig. 5.10

For Langmuir type adsorption with the same geometry and flow conditions, the concentration profiles are shown in Fig. 5.11.

Figure 5.12 depicts the concentration profiles for the realistic sorption mechanism with the same geometry and flow conditions as above.

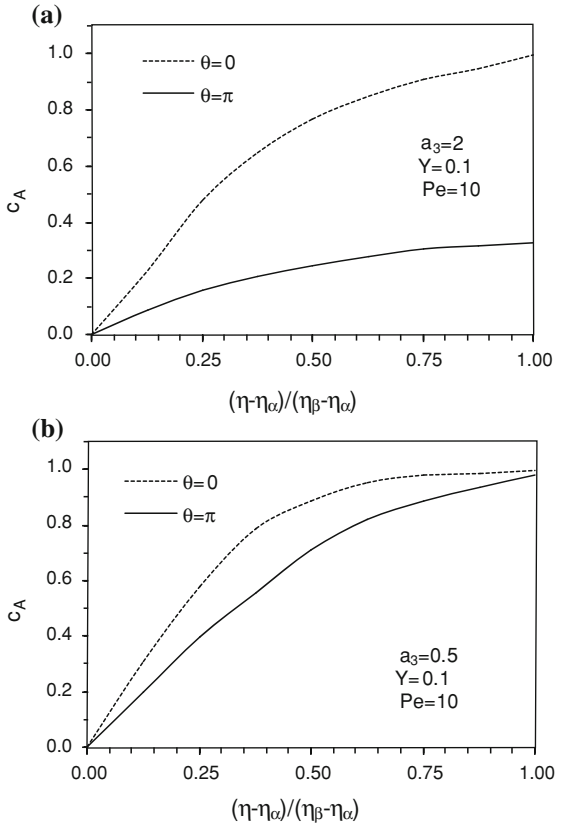

Fig. 5.10 Concentration profiles in the vicinity of adsorbing prolate (**a**) and oblate (**b**) spheroids-in-cell at three different angular positions for instantaneous adsorption and low Pe

Clearly, the results are qualitatively similar to those for spheres with the same transport and adsorption conditions.

For all the sorption mechanisms considered, and for the case of prolate spheroidal coordinates, the overall Sherwood number, Sh_o, is calculated as follows [9]:

$$Sh_o = \frac{1}{\left(1 + \dfrac{a_3}{a}\sin^{-1}\dfrac{a}{a_3}\right)} \int_{\pi}^{0} \left(\frac{\partial c_A}{\partial \eta}\right)_{\eta=\eta_a} \sin\theta \, d\theta \tag{5.44}$$

and, for oblate spheroidal coordinates [9]:

$$Sh_o = \frac{1}{\left(1 + \dfrac{\bar{a}_3^2}{2\bar{a}}\ln\dfrac{1+\bar{a}}{1-\bar{a}}\right)} \int_{\pi}^{0} \left(\frac{\partial c_A}{\partial \bar{\eta}}\right)_{\bar{\eta}=\bar{\eta}_a} \sin\theta \, d\theta \tag{5.45}$$

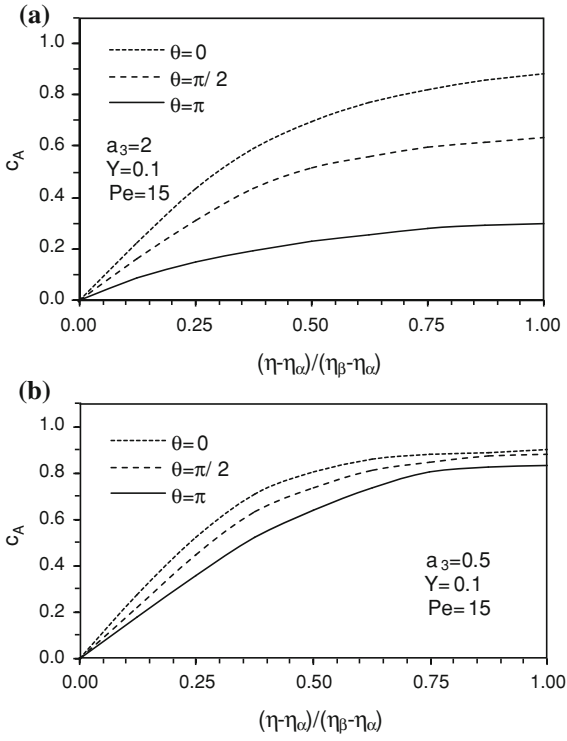

Fig. 5.11 Spatial concentration profiles at three different angular positions of the prolate (**a**) and oblate (**b**) spheroid-in-cell for Langmuir type adsorption $\left(\frac{k}{K}=1\right)$

Finally, the adsorption efficiency of prolate cells can be written as:

$$\lambda_0 = \frac{2}{Pe\, b_1^2} \int_{\pi}^{0} \left(\frac{\partial c_A}{\partial \eta}\right)_{\eta=\eta_a} \sin\theta \, d\theta \tag{5.46}$$

and

$$\bar{\lambda}_0 = \frac{2}{Pe\, \bar{b}_1^2} \int_{\pi}^{0} \left(\frac{\partial c_A}{\partial \bar{\eta}}\right)_{\bar{\eta}=\bar{\eta}_a} \sin\theta \, d\theta \tag{5.47}$$

The effect of the Peclet number on the Sherwood number for instantaneous adsorption is presented in Fig. 5.13.

As shown above, the boundary condition on the outer boundary is crucial for the estimation of macroscopic quantities such as the overall Sherwood number and adsorption efficiency. The dashed lines in Fig. 5.13 correspond to a "Levich-equivalent" approach, where a constant uniform concentration profile is considered on the surface of the outer spheroid. This condition is compatible with the assumption of a thin boundary layer (i.e. high Peclet regime), unless it breaks down when diffusion becomes significant and the boundary layer thickens. Indeed,

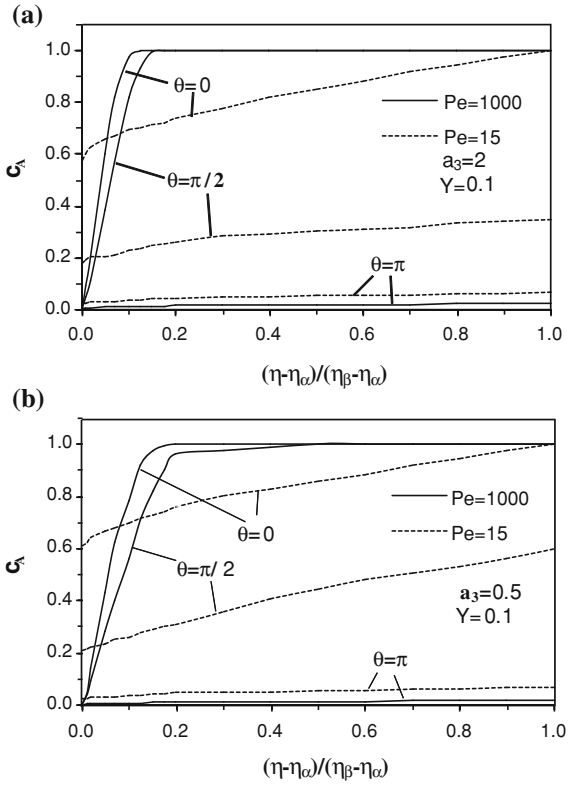

Fig. 5.12 Concentration profiles for prolate (**a**) and oblate (**b**) spheroidal shapes for high and low Peclet numbers at three different angular positions

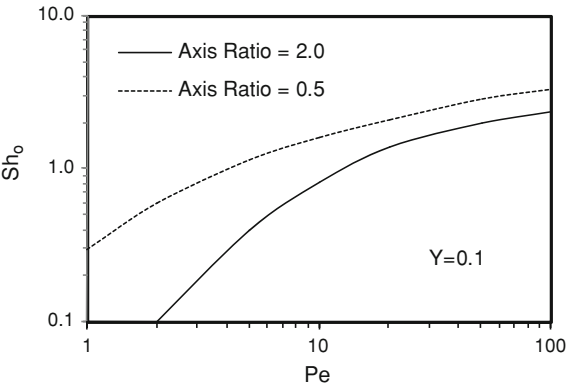

Fig. 5.13 Dependence of the overall Sherwood number on the Peclet for prolate and oblate spheroids-in-cell (instantaneous adsorption)

for $Pe \geq 20$ the Levich type approach predicts the correct Sh_o value with sufficient accuracy while, for lower Pe values, it yields Sh_o values weakly dependent on Pe, and converges to a limiting value as $Pe \to 0$. This limiting value is a function of porosity and the axis ratio, given by [9]:

$$Sh_0^* = 2a\left(1 + \frac{a_3^2}{a}\sin^{-1}\frac{a}{a_3}\right)^{-1}\left(\ln\frac{a+b_3}{b_1(a+a_3)}\right)^{-1} \tag{5.50}$$

for prolate spheroids-in-cell, and by:

$$Sh_0^* = 2\bar{a}\left(1 + \frac{\bar{a}_3^2}{2\bar{a}}\ln\frac{1+\bar{a}}{1-\bar{a}}\right)^{-1}\left(\tan^{-1}\frac{\bar{b}_3}{\bar{a}} - \tan^{-1}\frac{\bar{a}_3}{\bar{a}}\right)^{-1} \tag{5.51}$$

for oblate spheroids-in-cell. The above equations result from solving the Laplace equation, which is valid for the pure diffusive regime, i.e. as $Pe \to 0$ [5, 9]. However, conditions on the outer boundary (5.35) and (5.36) are obviously more consistent, resulting in more realistic Sh_o. For the realistic adsorption mechanism, typical analogous results are shown in Fig. 5.14.

In Fig. 5.14, a monotonic decrease of Sh_o, with increasing aspect ratio, is observed for all cases because prolate spheroids present higher diffusional resistance than oblate ones [6, 8]. Oblate spheroids present larger impact surface than prolate ones, and thus their capacity for adsorption is higher. This advantage of oblate shapes becomes very weak in the case of small Pe values because almost all the parts of the adsorbing solid surface become active as diffusion becomes dominant. For small Peclet values, unlike large ones, the overall Sherwood number depends appreciably on the order of the heterogeneous reaction because the concentration gradients become less significant. In this case, a decrease of Sh_o is observed when the reaction is of second-order (rather than first-order) as a higher reaction order causes lower concentration gradients and larger amounts of adsorbed mass. The overall Sherwood number can be 15–50% higher, depending on Pe, the shape, porosity, and order of the reaction, compared to the values obtained assuming instantaneous adsorption for either high or low Peclet values [8, 9]. This occurs because the concentration on the solid surface attains nonzero values and, thus, the difference $c_A(\eta_\beta, \theta) - c_A(\eta_a, \theta)$ becomes almost nil for some θ-values. The decrease of this driving force is significantly larger than the decrease of the concentration gradients observed when a realistic adsorption process is assumed rather than an instantaneous one.

Figure 5.15 presents adsorption efficiency results for prolate and oblate spheroids-in-cell, as functions of the Peclet number. The Levich approach on the outer boundary overestimates the adsorption efficiency for low Peclet values, leading to values larger than unity as $Pe \to 0$ for both geometries. On the contrary, the modification (5.35) and (5.36) predict λ_o values, which remain lower than unity even in the very low Pe range. What is observed in general is that convention is a favorable parameter allowing the escape of diluted material from the adsorbing solid surface.

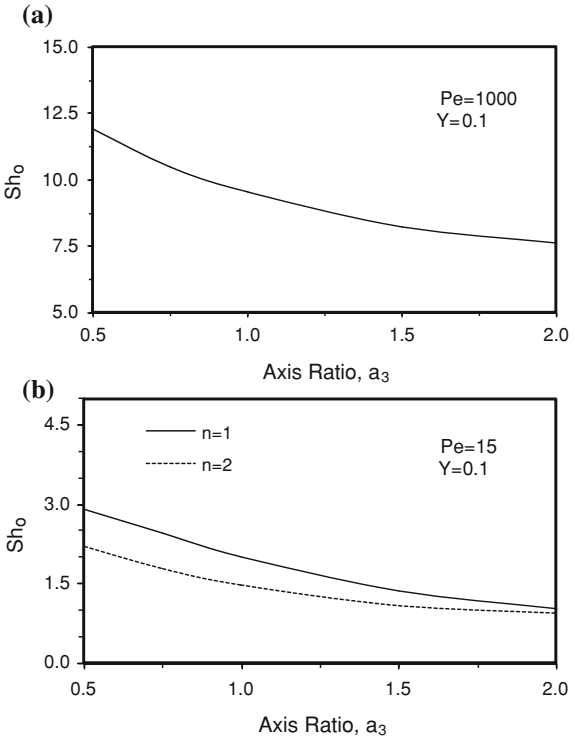

Fig. 5.14 Dependence of the overall Sherwood number on the axis ratio of the spheroid for a high (**a**) and a low (**b**) Peclet number (realistic adsorption)

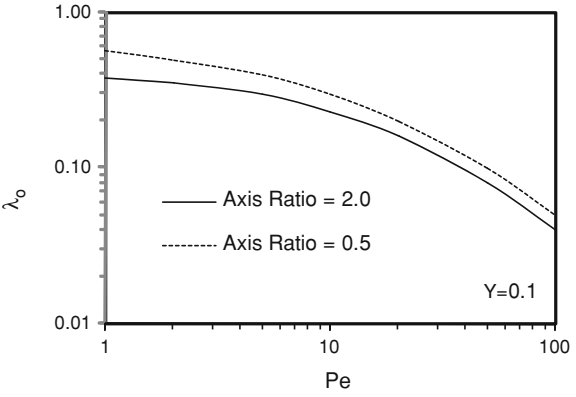

Fig. 5.15 Dependence of the adsorption efficiency on the Peclet number for prolate and oblate spheroids-in-cell (instantaneous adsorption)

The dependence of the overall adsorption efficiency on the Peclet number for both prolate (a) and oblate (b) geometry is given in Fig. 5.16, where the heterogeneous reaction is assumed to be either of first (n = 1) or second (n = 2) order. A significant decrease of the adsorption efficiency occurs as Pe increases. Values of overall adsorption efficiency obtained using the instantaneous adsorption model are 10–35% higher than those obtained here, because of the higher concentration gradients that instantaneous adsorption generates.

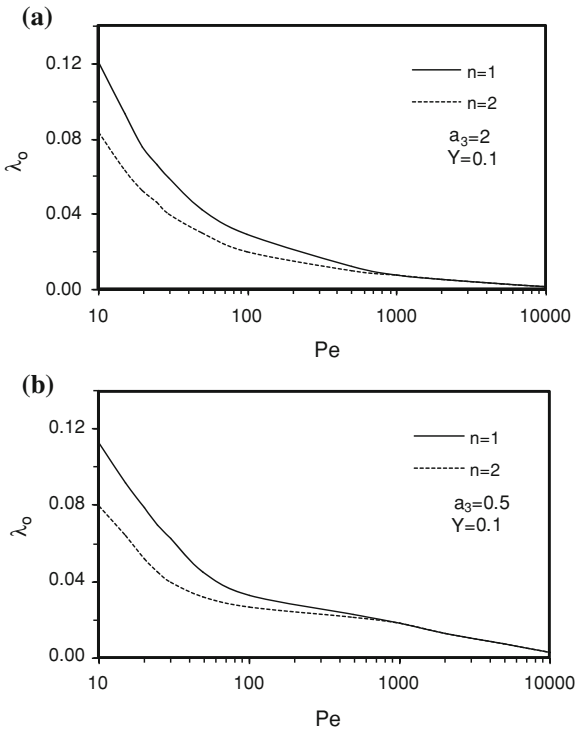

Fig. 5.16 Influence of the Peclet number on the adsorption efficiency for prolate (**a**) and oblate (**b**) spheroids-in-cell (realistic adsorption mechanism)

5.2.6 Single Phase Mass Transport in Other-Type Unit Cells

Further to the models described above, several unit cells have also been proposed in recent decades. These assemblies are all characterized by: (a) complex geometry which enforces numerical solutions of flow and transport problems, (b) the iteration of their structure to occupy the volume of interest (periodic boundary conditions), and (c) a high degree of freedom in the geometrical shapes considered to represent the real porous material. Increased computational power nowadays allows for the consideration of huge complex structures, therefore current research trends digress from the unit cell formulation, as analytical solutions no longer essential.

5.3 Single Phase Flow in Granular Structures

As described in Sect. 3.3, transport processes in granular media are of high scientific and technological interest, and mathematical modeling plays an important role in the in-depth study and understanding of these processes. In the majority of models on transport in granular media, the particles of the assemblage are assumed to adsorb mass instantaneously, which is obviously a fairly rare physicochemical phenomenon that pertains to a very limited range of applications. Only

recently have several detailed models of the sorption mechanism been presented for porous media processes [10, 13].

The aim of this Section is to present an adequate simulation for the adsorption heterogeneous reaction–desorption mechanism, which accurately describes the sorption upon a solid surface of a solute diluted in a flowing fluid [2, 20]. More specifically, it can be considered that the solute diluted in the bulk phase is initially adsorbed by the solid surface where a heterogeneous reaction takes place and its products, assumed to be inactive and of very low concentrations, are again desorbed in the bulk phase. The adsorption is assumed to occur due to vacant sites that are normally distributed over the surface area, while the whole process is determined by an overall rate according to the flow regime and thermodynamics [25].

As described in Sect. 3.3, the procedure of random deposition under specific restrictions must be followed in order to represent the stochastically constructed three-dimensional assemblages of spheres which are considered a typical demonstration of a granular medium (see Fig. 3.7). The flow-field within such an assemblage is typically obtained by the numerical solution of the Stokes equations coupled with the continuity equation, as described in Sect. 3.3.

Assuming no reactions occur in the bulk phase, the time-dependent mass transport of a passive solute (namely, component A) in the stochastically constructed medium is described by the convection–diffusion equation:

$$\frac{\partial c_A}{\partial t} + \nabla \cdot (\mathbf{u} c_A) = D \nabla^2 c_A \tag{5.52}$$

To investigate the importance of the adsorption mechanism in such complex structures, all the previously discussed different adsorption mechanisms are adopted here. Neutral solid surfaces again lack scientific and engineering interest. The other sorption mechanisms considered are instantaneous adsorption (5.8), adsorption under the Langmuir isotherm (5.9)–(5.11), and the realistic sorption mechanism (5.13)–(5.15). Typical conditions are also considered at the other boundaries.

The validity of the solution scheme for the mass transport problem can be checked in the limiting case of a periodic array of spheres with radius R, which is fed at $x = 0$ by a concentration pulse. The concentration profile with time at the outlet $\left(x = L = \frac{51}{8} R \right)$ is then expressed as [23]:

$$c(t) = \frac{1}{\sqrt{4\pi D^* t}} \exp\left[\frac{-(L - \langle u \rangle t)^2}{4 D^* t} \right] \tag{5.53}$$

where $\langle u \rangle$ is the average fluid velocity, and D^* the dispersion coefficient. Therefore, the dimensionless time (defined by using $\frac{L^2}{D^*}$ as characteristic time) at which the maximum outlet concentration is recorded can be calculated as:

$$t_{\max} = \frac{\left(\sqrt{1 + Pe^2} - 1 \right)}{Pe^2} \tag{5.54}$$

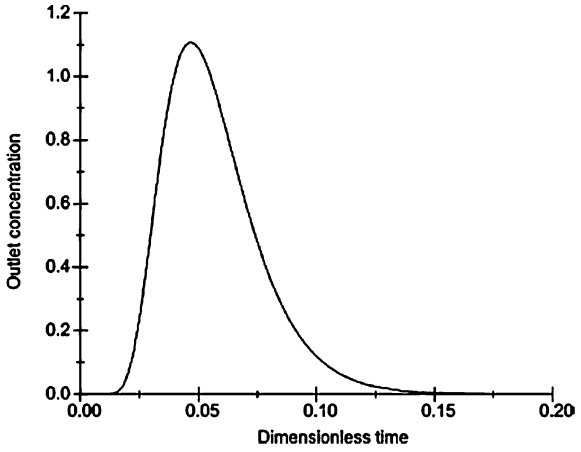

Fig. 5.17 Outlet concentration profile for Pe = 20 in a periodic array of spheres

where $Pe = \dfrac{\langle u \rangle L}{D}$ is the Peclet number.

The dispersion coefficient can be determined based on the approach of Salles et al. [24] and in these simulations is found to be $D^* = 1.34D$, thus giving $t_{\max} = 0.047$ for $Pe = 20$, when the numerically calculated value is 0.048 (see Fig. 5.17).

Note that the dimensionless time step dt must be small enough ($<10^{-5}$) to attain acceptable accuracy in the calculations.

The spatial distribution of the concentration, obtained numerically for $Pe = 20$ and $\varepsilon = 0.7243$ along the flow direction, is presented in Fig. 5.18 where a randomly selected two-dimensional cut of the stochastically constructed medium is visualized for both instantaneous and Langmuir-type adsorption. The concentration is higher on the left side of the images (inlet) and gradually decreases across the medium in a manner significantly steeper for the instantaneous than the Langmuir-type adsorption. The adsorption efficiency for several porosities ($\varepsilon = 0.9883$, $\varepsilon = 0.8136$ and $\varepsilon = 0.7243$) and Peclet numbers was calculated by the full-numerical scheme in the sphere assembly for both instantaneous and Langmuir-type adsorption and presented in Fig. 5.19. The effects of porosity and Peclet on the adsorption efficiency are the same as those above (higher efficiencies correspond to lower porosity, and increasing Peclet numbers lead to lower λ_0 values). Instantaneous adsorption leads to higher adsorption efficiency values than those calculated under other adsorption mechanisms with the same Peclet number and porosity.

The effect of the k/K ratio used in the boundary condition for Langmuir-type adsorption, on the computed adsorption efficiency is presented in Fig. 5.20 for $Pe = 20$ and $\varepsilon = 0.8136$. As this ratio increases, a significant increase of λ_0 is observed because higher k/K corresponds to lower ratios of the covered surface, Θ_{eq}. This, in turn, corresponds to lower surface concentrations and higher concentration gradients, i.e. to higher λ_0. On the other hand, an increased k/K ratio can be viewed as a higher adsorption rate for a given K value and therefore, less mass of substance A can escape from the solid surfaces resulting in higher λ_0 values.

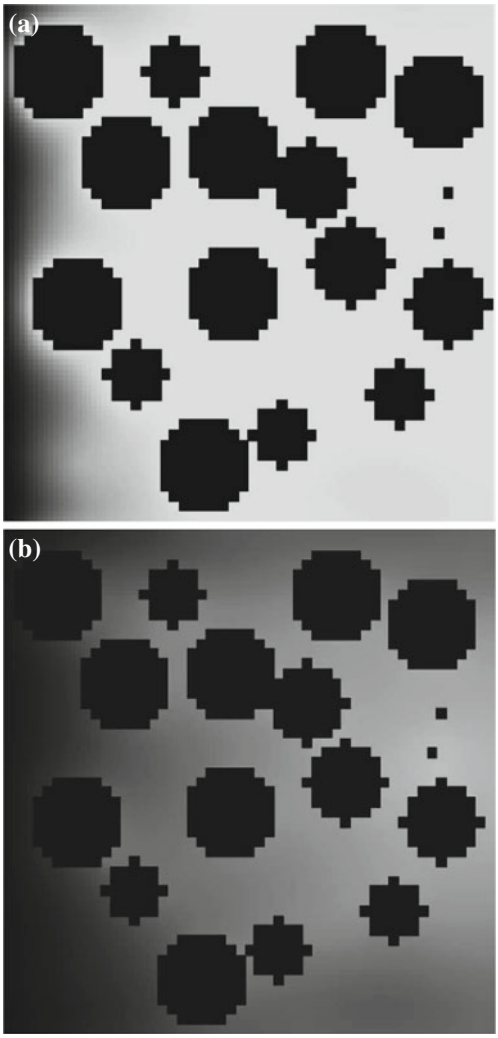

Fig. 5.18 Spatial distribution of the concentration of substance A within a two-dimensional cut of the three-dimensional sphere assemblage for **a** instantaneous and **b** Langmuir-type adsorption. (The flow inlet is on the left side. *Darker areas* correspond to higher concentrations.)

It is interesting to consider the relative agreement between the results produced by considering the sphere-in-cell approximation and those obtained from the numerical solution of the three-dimensional sphere assemblages. Figure 5.21a compares the respective adsorption efficiencies and instantaneous adsorption for porosity approaching unity ($\varepsilon = 0.9883$). The agreement is perfect as the semi-analytical sphere-in-cell model can adequately predict reality for such high porosity values. When lower porosities are considered, the fundamental assumptions of the sphere-in-cell approximation are less satisfactory. Indeed, in the low *Pe* regime characterized by the gradual dominance of the diffusive over the convective terms, the semi-analytical approach of the sphere-in-cell model cannot adequately describe the mass transport process, as the diffusion layer is very thick

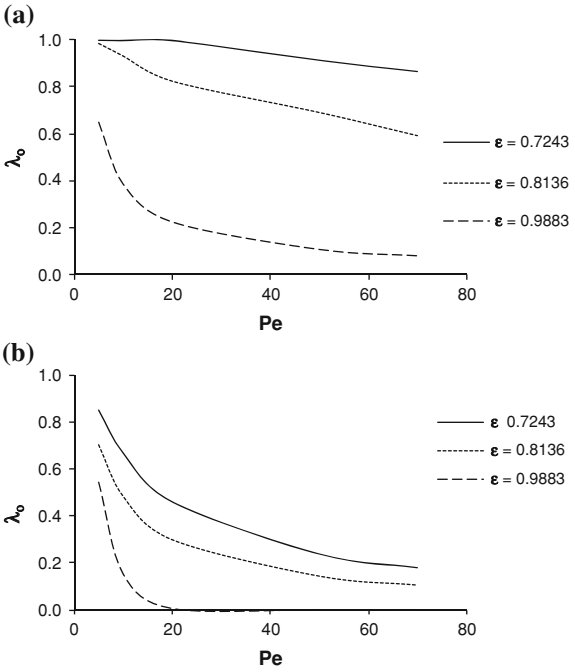

Fig. 5.19 Adsorption efficiency of the three-dimensional sphere assemblage as a function of Pe for various porosities in **a** instantaneous and **b** Langmuir-type adsorption

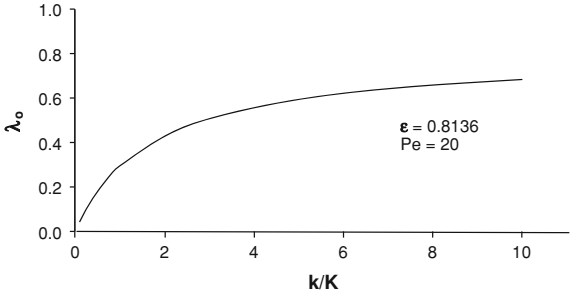

Fig. 5.20 The effect of k/K ratio on adsorption efficiency

(larger than the cell itself) and tends to infinity as $Pe \rightarrow 0$. On the other hand, as Pe increases, flow becomes more convective and the analytical flow-field of the sphere-in-cell is no longer a sufficient approximation of the actual flow-field in real granular media, thus leading to model discrepancies. However, for $\varepsilon = 0.8136$ and $\varepsilon = 0.7243$ the agreement between the two approaches ranges from very good to satisfactory depending on the Pe range considered. This result is expected since both the sphere-in-cell and sphere assemblage geometries used in the present study were constructed to be characterized by the same porosity and internal (adsorbing) surface area. This was accomplished by selecting the correct radius and sphere population number in the assemblage. Of course, it is possible to construct several sphere assemblages of the same porosity but with varying sphere radius and

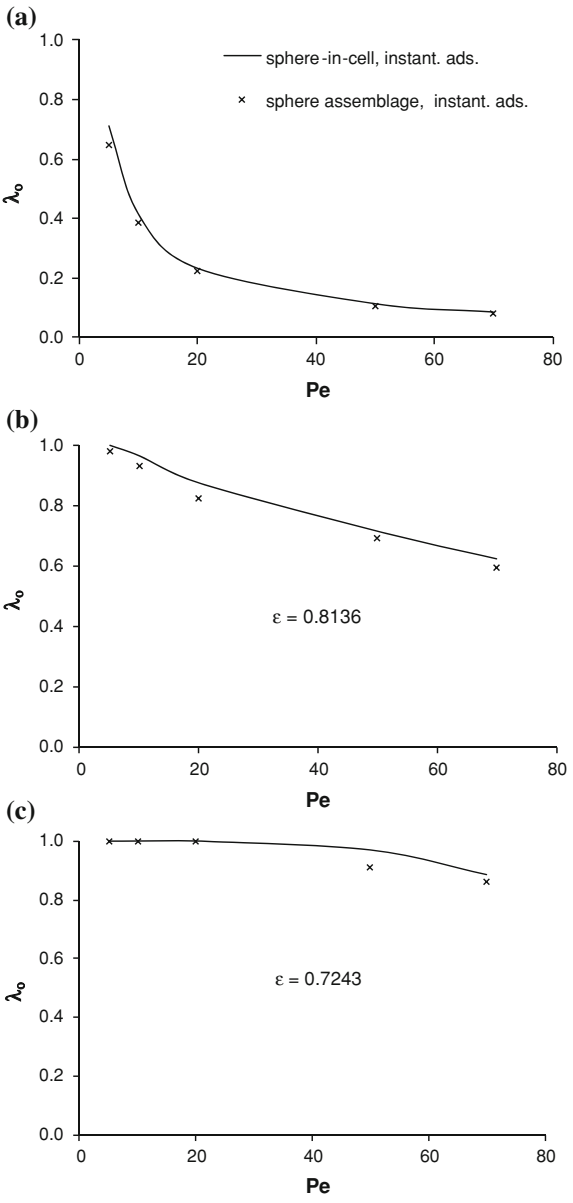

Fig. 5.21 Comparison between adsorption efficiency in sphere-in-cell and sphere assemblies for different porosities

population number and therefore with different internal surfaces. Figure 5.22 shows how these different arrangements of spheres affect the calculated adsorption efficiency for instantaneous and Langmuir adsorption. The horizontal axes represent the internal surface ratio which changes when different media are considered. The case of adsorption surface ratio equal to unity corresponds to the results discussed so far. Evidently under instantaneous adsorption conditions λ_0 is not

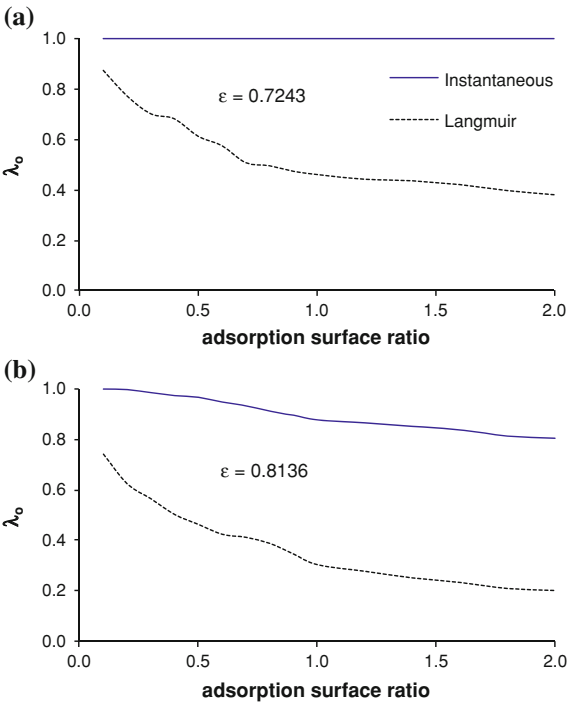

Fig. 5.22 The effect of using sphere assemblages with varying internal surface area on adsorption efficiency and for two porosity values: 0.7243 (**a**) and 0.8136 (**b**)

influenced significantly by changes in the medium. This is again due to the high concentration gradients prevailing that mask the effect of internal surface variation. However, in the more realistic Langmuir-type of adsorption a very pronounced influence on λ_0 is observed implying that caution should be exercised when using the sphere-in-cell model to determine adsorption efficiency in granular media. This strongly indicates that matching porosity alone is not sufficient for a reliable result.

5.4 Macroscopic Quantities for Single Phase Transport

There are many industrial and technological applications of mass transport within porous media in a variety of scientific fields, such as environment, energy, biology, etc. [15, 18, 27]. Mathematical modeling of transport processes in porous med,ia is a powerful tool, especially whenever experimental observations are difficult, time consuming and expensive. Due to the coupling between the physicochemical mechanisms and the local geometry of the porous medium mathematical descriptions of mass transport in realistic porous media are highly complex. Modeling becomes more difficult when moving from the pore level to the field level, because different length scales result in complicated descriptions of the problem's physics and therefore increased computational power is usually required.

From the late 1950s, special effort has been given to mathematically describe and solve flow and mass transport problems in porous media. Initially quite simplified geometries were considered, where analytical solutions can be obtained for the flow field and the mass diffusion and/or adsorption process (see previous chapters on cell models). Numerical solutions in realistic reconstructions of porous media for the Stokes equations and related transport problems have been obtained for several specific applications during the last decades [1, 3, 16, 19, 26]. In the majority of these works, the particles were assumed to adsorb mass instantaneously however, this is a rare physicochemical phenomenon that pertains to a very limited range of applications. Recently, further detailed models of the sorption mechanism have been presented for porous media processes.

This Section aims to simulate an adsorption—heterogeneous reaction—desorption mechanism for a complex granular porous geometry that can accurately describe the sorption upon a solid surface of a solute diluted in the flowing fluid [2, 20]. Details about this sorption mechanism can be found in Sect. 5.2.

The major issue of typical macroscopic modeling for such, or simpler, cases can be identified at the a priori definition of the macroscopic quantities necessary to solve these equations, although they are normally derived from the solution of these equations. So far, mainly empirical or semi-empirical correlations for these parameters have been proposed based on experimental measurements of specific systems [5, 22]. The generalized treatment of such a problem corresponds to theoretical estimations of these quantities where the volume averaging concept is a frequently employed tool for large-scale modeling of processes taking place in porous media, thus eliminating the influence of porous geometry on the transport results [28, 30, 31]. Starting with transport equations at the micro-scale (pore) level, the spatial averaging theorem is applied with the correct assumptions, leading to the estimation of macroscopic quantities such as mass transfer coefficient and dispersion tensor [21]. To further simplify the modeling and eliminate the simulation effort, the majority of the above-mentioned models have been applied to simplistic domains, such as unit cells, since the focus was on the interfacial mass exchange rather than the representation of the medium in a realistic manner.

5.4.1 Stochastically Constructed 3-D Sphere Assemblage

Representation of the biphasic domains under consideration is achieved by the random deposition of spheres of a given radius in a box of specified length. (For specific details on the efficient algorithm (ballistic deposition) used for the domain's stochastic construction, see Sect. 3.3).

5.4.2 The Flow Field (Single Phase Flow)

The velocity field is computed numerically by solving the Stokes equations as described previously (see Sect. 3.3).

5.4.3 Mathematical Formulation

The area of interest is a porous domain consisting of a flowing aqueous phase (L-phase) and a solid phase (S-phase). A tracer is advected by the flowing liquid phase, being sorpted in the liquid–solid interface. The governing processes are diffusion and advection in the liquid phase, and the liquid–solid interface is characterized by the realistic adsorption/reaction/desorption mechanism of the tracer (see below).

Assuming that the bulk phase is chemically neutral, the pore-level transport of the tracer in the β-phase is described by the convection–diffusion equation:

$$\frac{\partial C_L}{\partial t} + \nabla \cdot (\mathbf{v} C_L) = D_L \nabla^2 C_L \tag{5.55}$$

where C_L is concentration, t is time, $\mathbf{v}$ is the fluid velocity, and D_L is the diffusivity in the liquid phase.

To ensure the continuity of the mass fluxes on the solid–liquid interfaces, the following boundary condition (similar to Eq. 5.13) is applied:

$$\mathbf{n}_{LS} \cdot \nabla C_L = R_n, \text{ at the solid}-\text{liquid interface } A_{LS} \tag{5.56}$$

where the overall sorption rate R_n is dependent on the type of sorption process considered. In accordance to Sect. 5.2, the rate R_n is given as:

$$R_n = k_s C_{LS}^n \tag{5.57}$$

where the concentration of the tracer upon the solid surface, C_{LS}, is described by the relation:

$$k_s C_{LS}^n + [k_d + k_a C_L N] C_{LS} - k_a C_L \xi_m = 0 \tag{5.58}$$

5.4.4 The Volume-Averaging Procedure

Following the volume-averaging procedure [22], local concentrations and velocities are next decomposed into interstitial averages and fluctuations

$$C_L = \langle C_L \rangle^L + C_L' \tag{5.59}$$

$$\mathbf{v} = \langle \mathbf{v} \rangle^L + \mathbf{v}' \tag{5.60}$$

which are subsequently substituted in the governing differential equations. Invoking separation of scales to discard small terms, linearizing and following Quintard and Whitaker [22], assuming an isotropic medium of uniform porosity and constant volume fractions, the following representation is obtained:

$$C_L' = \mathbf{b} \cdot \nabla \langle C_L \rangle^L - s_L \langle C_L \rangle^L \tag{5.61}$$

where **b** and s_L are closure variables satisfying specific boundary value problems.

It can be readily shown that variable s of the β-phase satisfies the boundary value problem:

$$\mathbf{v} \cdot \nabla s_L = D\nabla^2 s_L - \varepsilon^{-1}\alpha \tag{5.62}$$

with

$$\mathbf{n}_{LS} \cdot \nabla s_L = 0, \text{ at the solid}-\text{liquid interface } A_{LS} \tag{5.63}$$

and

$$\langle s_L \rangle = 0 \tag{5.64}$$

The mass-transfer coefficient, α, on Eq. 5.62, is given by:

$$\alpha = \frac{D}{V} \int\limits_{A_{LS}} \mathbf{n}_{LS} \cdot \nabla s_L dA \tag{5.65}$$

The above can be simplified by introducing the transformation $s_L = 1 + \alpha\psi_{L\sigma}$ and in dimensionless form:

$$s_L = 1 + \alpha^* \zeta_L \tag{5.66}$$

where the dimensionless mass-transfer coefficient is defined as:

$$\alpha^* = \frac{a l_L^2}{D} \tag{5.67}$$

and l_L denotes the characteristic length of the liquid phase. In dimensionless notation, the boundary value problems then read as follows:

$$Pe\ \mathbf{u} \cdot \nabla \zeta_L = \nabla^2 \zeta_L - \varepsilon_L^{-1} \text{ in the liquid phase} \tag{5.68}$$

$$\mathbf{n}_{LS} \cdot \nabla \zeta_L = r_n \text{ at the solid}-\text{liquid interface } A_{LS} \tag{5.69}$$

where $Pe = \frac{\langle \mathbf{u} \rangle^L l_L}{D}$ is the Peclet number defined in the liquid phase, **u** is the dimensionless velocity vector, ζ_L is the scalar variable used for the decomposition, and r_n is the dimensionless sorption rate.

Following the above, the dimensionless mass transfer coefficient simply becomes:

$$\alpha^* = -\frac{\varepsilon}{\langle \zeta_L \rangle} \tag{5.70}$$

Brackets denote averages over the total volume V or the volume of the aqueous phase, V_L, where the superficial volume average is defined as:

$$\langle y_L \rangle = \frac{1}{V} \int\limits_{V_L} y_L dV \tag{5.71}$$

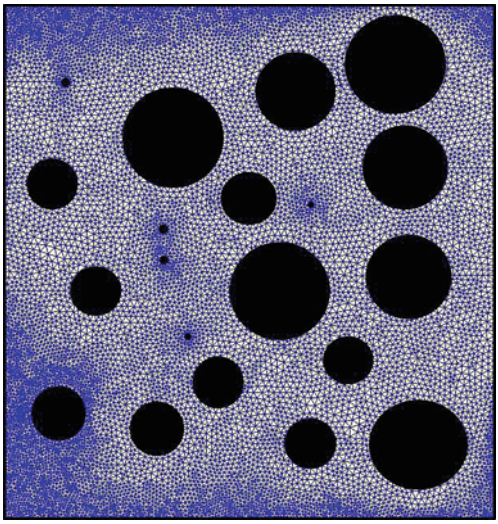

Fig. 5.23 A selected two-dimensional cut of the simulated geometry discretized by an unstructured grid

and the interstitial volume average as:

$$\langle y_L \rangle^L = \frac{1}{V_L} \int_{V_L} y_L dV \tag{5.72}$$

5.4.5 Simulations

To adequately simulate the above-described problem, an algorithmic procedure has been developed as follows:

- Solve the flow problem at the pore level and calculate interstitial and superficial velocity fields
- Formulate the mass transport problem at the pore level
- Decompose the local velocity and concentration in terms of an interstitial average and a fluctuation
- Describe the concentration fluctuations in terms of linear combinations of interstitial averaged concentration and its gradient
- Solve the closure problem
- Integrate the resulting quantities to calculate macroscopic coefficients.

The numerical scheme used for all the simulations is described in Sect. 3.3 and a typical grid representation is depicted in Fig. 5.23 (for the same two-dimensional cut as the previous Fig. 5.18).

Table 5.1 Independence on random deposition ($\varepsilon = 0.43$).

Different random assemblages	*Pe*	***n***	a^*
Case 1	1	1	20.93
Case 2	1	1	20.83
Case 3	1	1	21.01
Case 4	1	1	20.77
Case 5	1	1	20.96
Case 1	100	1	46.55
Case 2	100	1	45.87
Case 3	100	1	46.11
Case 4	100	1	47.02
Case 5	100	1	46.39
Case 1	1	2	19.36
Case 2	1	2	19.91
Case 3	1	2	19.07
Case 4	1	2	18.66
Case 5	1	2	19.12
Case 1	100	2	45.88
Case 2	100	2	45.01
Case 3	100	2	46.99
Case 4	100	2	45.85
Case 5	100	2	46.02

5.4.6 Results and Discussion

The results were initially validated against the randomness of the structure, as previously discussed. More precisely, the mass transfer coefficient a^* was calculated for several different depositions of spheres while the porosity value was kept constant (=0.43). It was found that the random deposition does not significantly affect mass transfer to the solid phase, as shown in Table 5.1, where each "case" corresponds to a different deposition of a variable number of spheres of different radii, and porosity is kept constant in all cases. (Five different cases were chosen for the same porosity to verify whether the results were independent of the medium construction). Solution dependence on the grid was also examined in terms of the mass transfer coefficient. It was found that the discretization used is more than sufficient for adequate calculations. It should be noted that the parametric analysis of the grid influence is limited to only reaction order, as this parameter introduces non-linearity, thus the solution it is depended on this reaction order.

The relative agreement between the results produced by considering the approximation presented in Sect. 5.3 and those obtained using the above technique is presented in Fig. 5.24. By assuming a typical value of ξ_m (1 active site per Å^2), the values of the sorption constants were (before the non-dimensionalization of the problems) $k_a = 1 \times 10^{-30}$ m^{3}sec^{-1}, $k_d = 8 \times 10^{-3}$ sec^{-1} and $k_s = 8 \times 10^{-3} \times 100^{(1-n)}$ (kg m^{-2})$^{1-n}$sec^{-1}. These values can be considered as typical [2] and are used in the

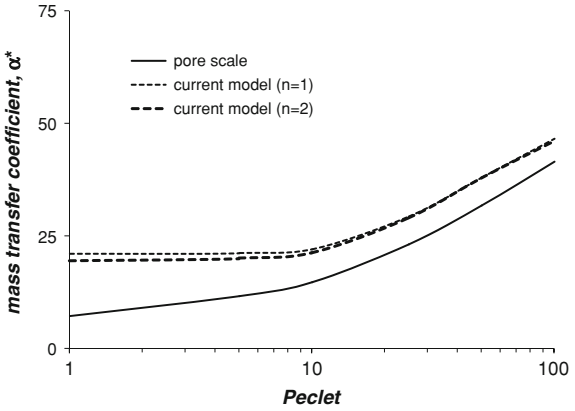

Fig. 5.24 Comparison between the results of the current model and those found in the literature

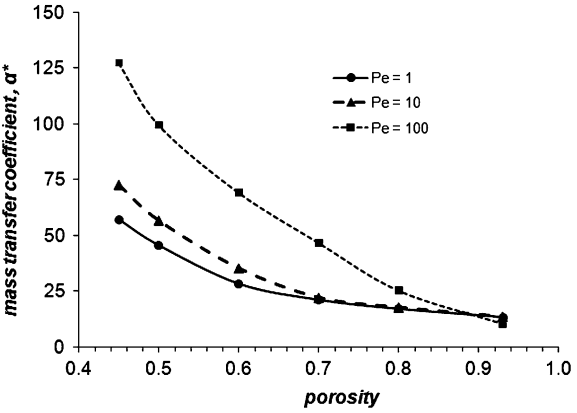

Fig. 5.25 The influence of porosity on mass transport

simulations presented here unless otherwise stated. Figure 5.24 compares the respective mass transfer coefficient for the standard porosity $\varepsilon = 0.43$ while the realistic adsorption/reaction/desorption mechanism includes the heterogeneous reaction of first (n = 1) and second (n = 2) order. Regarding the pore-level simulations, a discrepancy from the results of the current model is always observed, thus indicating the underestimation of macroscopic mass transport quantities when calculated using pore-level approaches in small-scale domains [7].

In terms of physical interpretation, Fig. 5.24 depicts the effect of convection on mass transport. It can be seen that the stronger the convection, the more efficient the tracer transport from the fluid to the solid phase, at least for low and intermediate porosity values, which correspond to relatively high amounts of active solid absorbers in the medium and absorb the tracer. Finally, the order of the reaction does not seem to significantly affect the results, or the agreement between the two approaches. Only the first order reaction is considered hereafter.

The influence of the medium's volume porosity on mass transport is presented in Fig. 5.25. It is clear that porosity is an unfavorable parameter for adsorption,

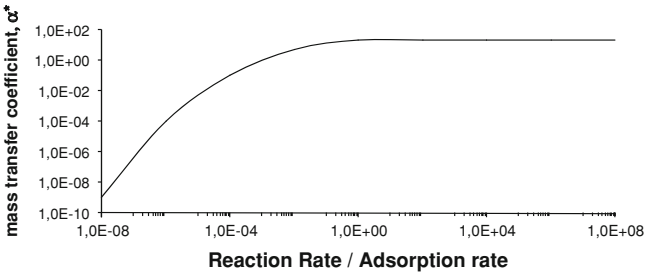

Fig. 5.26 Dependence of mass transport on the ratio of the reaction to the adsorption rates

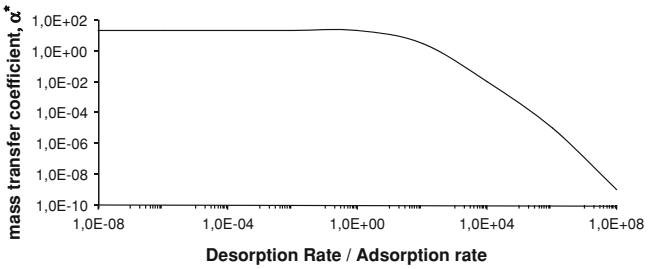

Fig. 5.27 Dependence of mass transport on the ratio of desorption to adsorption rates

since void space increases as porosity increases (although the active solid surface area does not necessarily decrease), thus corresponding to high possibility for the tracer to escape from the porous material through the void space. For high porosity values, as Peclet values increase, the transport process becomes more and more convective, thus mass transport becomes less effective, i.e. high amounts of the tracer can escape from the medium. On the other hand, low porosity values correspond to large amounts of solid phase in the medium, thus convection favors mass transport since the tracer is forced to approach the absorbing surfaces. These two competitive phenomena are shown by the cross of the curves in Fig. 5.25, which correspond to a porosity value where both mechanisms are of equal strength. This value obviously depends on the specific flow and transport characteristics.

Figures 5.26 and 5.27 depict the relative influence of the sorption mechanism, i.e. the reaction, adsorption and desorption rates, on mass transport. More precisely, Fig. 5.26 presents the mass transfer coefficient as a function of the ratio of tracer destruction rate due to the reaction, divided by the tracer destruction rate due to adsorption. In any case, the values of the rate constants not involved in these ratios were kept standard. It is observed that the decrement of the reaction rate (for constant adsorption rate) corresponds to a consequent decrement of mass transport because the tracer has been adsorbed but not destroyed at the same rate and, therefore remains on the surface filling the vacant sites, i.e. setting barriers in

the tracer sorption process. The increased reaction rate forces adsorption to tend asymptotically to a constant value which depends on the geometrical characteristics of the medium. Figure 5.27 shows the influence of the ratio desorption/adsorption rate on mass transport for a heterogeneous reaction of the first order. It is observed that increasing the desorption rate beyond a critical value corresponds to a decrease in mass transport. It is important to note that the value attained by the mass transfer coefficient before the critical desorption rate is the same as the asymptotic value of Figure 5.26, thus further underlying its independence on the reaction characteristics.

References

1. Ahmadi, A., Aigueperse, A., Quintard, M.: Calculation of the effective properties describing active dispersion in porous media: from simple to complex porous media. Adv. Water Resour. **24**, 423–438 (2001)
2. Atkins, P., de Paula, J.: Physical Chemistry, 7th edn. Oxford University Press, Oxford (2002)
3. Bekri, S., Thovert, J.F., Adler, P.M.: Dissolution and deposition in fractures. Eng. Geo. **48**, 283–308 (1997)
4. Bird, R.B., Stewart, W.E., Lightfoot, E.N.: Transport Phenomena. Wiley, New York (1960)
5. Burganos, V.N., Coutelieris, F.A., Payatakes, A.C.: Sherwood number for mass transfer to a swarm of adsorbing spheroidal particles at any Peclet number. AIChE J. **43**, 844–848 (1997)
6. Coutelieris, F.A.: The influence of axial orientation of spheroidal particles on the adsorption rate in a granular porous medium. Stud. Surf. Sci. Catal. **144**, 745–751 (2002)
7. Coutelieris, F.A.: Modeling of flow and mass transport in granular porous media. Cent. Eur. J. Phys. **9**, 962–968 (2011)
8. Coutelieris, F.A., Burganos, V.N., Payatakes, A.C.: On mass transfer from a newtonian fluid to a swarm of adsorbing spheroidal particles for high Peclet numbers. J. Colloid Interface Sci. **161**, 43–52 (1993)
9. Coutelieris, F.A., Burganos, V.N., Payatakes, A.C.: Convective diffusion and adsorption in a swarm of spheroidal particles. AIChE J. **41**, 1122–1134 (1995)
10. Coutelieris, F.A., Burganos, V.N., Payatakes, A.C.: Model of adsorption–reaction–desorption in a swarm of spheroidal particles. AIChE J. **50**, 779–785 (2004)
11. Coutelieris, F.A., Kainourgiakis, M.E., Stubos, A.K.: The effect of the porosity on the adsorption rate in granular porous media. Stud. Surf. Sci. Catal. **144**, 753–760 (2002)
12. Coutelieris, F.A., Kainourgiakis, M.E., Stubos, A.K.: Low Peclet mass transport in assemblages of spherical particles for two different adsorption mechanisms. J. Colloid Interface Sci. **264**, 20–29 (2003)
13. Coutelieris, F.A., Kainourgiakis, M.E., Stubos, A.K.: Low to moderate Peclet mass transport in assemblages of spherical particles for a realistic adsorption–reaction–desorption mechanism. Powder Tech. **159**, 173–179 (2005)
14. Dassios, G., Hadjinicolaou, M., Payatakes, A.C.: Generalized eigenfunctions and complete semiseparable solutions for stokes flow in spheroidal coordinates. Quart. Appl. Math. **52**, 157–191 (1994)
15. Ellis, T.G., Eliosov, E., Schmit, C.G., Jahan, K., Park, K.Y.: Activated sludge and other aerobic suspended culture processes. Water Environ. Res. **74**, 385–410 (2002)
16. Kapellos, G.E., Alexiou, T.S., Payatakes, A.C.: A multiscale theoretical model for diffusive mass transfer in cellular biological media. Math. Biosci. **210**, 177–237 (2007)
17. Levich, V.G.: Physicochemical Hydrodynamics. Pentice-Hall, Englewood Cliffs (1962)
18. Meakin, P., Skjeltorp, A.T.: Application of experimental and numerical models to the physics of multiparticle systems. Adv. Phys. **42**, 1–127 (1993)

19. Mourzenko, V.V., Bekri, S., Thovert, J.F., Adler, P.M.: Deposition in fractures. Chem. Eng. Commun. **150**, 431–464 (1996)
20. Peters, M.H., Jalan, R.K., Gupta, D.: A dynamic simulation of particle deposition on spherical collectors. Chem. Eng. Sci. **40**, 723–731 (1985)
21. Quintard, M., Whitaker, S.: Transport in ordered and disordered porous media: volume averaged equations, closure problems and comparison with experiments. Chem. Eng. Sci. **48**, 2537–2564 (1993)
22. Quintard, M., Whitaker, S.: Convection, dispersion and interfacial transport of contaminants: Homogeneous porous media. Adv. Water Resour. **17**, 221–239 (1994)
23. Sahimi, M.: Flow phenomena in rocks: from continuum models to fractals, percolation, cellular automata, and simulated annealing. Rev. Mod. Phys. **65**, 1393–1534 (1993)
24. Salles, J., Thovert, J.F., Delannay, R., Prevors, L., Auriault, J.L., Adler, P.M.: Taylor dispersion in porous media. Determination of the dispersion tensor. Phys. Fluids A - Fluid **5**, 2348–2367 (1993)
25. Smith, J.M.: Chemical Engineering Kinetics. McGraw-Hill, Tokyo (1981)
26. Tardos, G.I., Gutfinger, C., Abuaf, N.: High Peclet mass transfer to a sphere in a fixed or fluidized bed. AIChE J. **22**, 1147–1150 (1976)
27. Valdes-Parada, F.J., Ochoa-Tapia, J.A., Alvarez-Ramirez, J.: Effective medium equations for fractional fick's law in porous media. Phys. A **373**, 339–353 (2007)
28. Whitaker, S.: Diffusion and dispersion in porous media. AIChE J. **13**, 420–427 (1967)
29. Wilson, E.J., Geankoplis, C.J.: Liquid mass transfer at very low reynolds numbers in packed beds. Ind. Eng. Chem. Fund **5**, 9–14 (1966)
30. Zanotti, F., Carbonell, R.G.: Development of transport equations for multiphase systems I: general development for two-phase systems. Chem. Eng. Sci. **39**, 263–278 (1984)
31. Zanotti, F., Carbonell, R.G.: Development of transport equations for multiphase systems II: application to one-dimensional axi-symmetric flows of two-phases. Chem. Eng. Sci. **39**, 279–297 (1984)